Synthesis and full characterization of the phase-pure pyrochlore $Ce_2Zr_2O_7$ and the κ-$Ce_2Zr_2O_8$ phases

Sven Urban [a], Paolo Dolcet [b], Maren Möller [a], Limei Chen [c], Peter J. Klar [c], Igor Djerdj [d], Silvia Gross [b], Bernd M. Smarsly [a,*], Herbert Over [a,*]

[a] *Physikalisch-Chemisches Institut, Justus-Liebig-University, Heinrich-Buff-Ring 17, 35392 Giessen, Germany*
[b] *Istituto per l'Energetica e le Interfasi, IENI-CNR, Dipartimento di Scienze Chimiche, Università degli Studi di Padova, via Francesco Marzolo, 1, I-35131 Padova, Italy*
[c] *I. Physikalisches Institut, Justus Liebig University, Heinrich-Buff-Ring 16, 35392 Giessen, Germany*
[d] *Department of Chemistry, J. J. Strossmayer University of Osijek, Ulica cara Hadrijana 8/a, HR-31000 Osijek, Croatia*

A B S T R A C T

The κ-$Ce_2Zr_2O_8$ phase has been synthesized starting from t-$Ce_{0.5}Zr_{0.5}O_2$ solid solution which is reduced by hydrogen at high temperatures to form the pyrochlore $Ce_2Zr_2O_7$ phase (pyr-$Ce_2Zr_2O_7$) with high degree of ordering of the cationic sublattice. The final step in the synthesis of the κ-$Ce_2Zr_2O_8$ phase includes a mild re-oxidation of pyr-$Ce_2Zr_2O_7$ at around 600 °C under atmospheric conditions. Yet, the synthesis of phase-pure κ-$Ce_2Zr_2O_8$ phase (phase-pure and with highest ordering) is still not settled since most of the previous studies used reduction temperatures of 1300 °C and below. We show in this contribution that 1300 °C is not sufficient to warrant the preparation of phase-pure pyr-$Ce_2Zr_2O_7$ and κ-$Ce_2Zr_2O_8$, but that rather temperatures as high as 1500 °C are required to assure phase purity of both phases. This conclusion is drawn from extended X-ray diffraction and X-ray absorption spectroscopy analyses together with Raman spectroscopy, providing in-depth details of the structure on the level of both, the evolution of the special periodic structure and the coordination of the metal atoms.

© 2016 Elsevier B.V. All rights reserved.

1. Introduction

CeO$_2$-based materials are employed in a variety of different applications in catalysis [1] acting as carrier for the active metal particles, as oxygen storage co-catalysts in exhaust gas post-treatment in automobiles, or even as a catalytically active component (with no noble metals being involved) such as in the catalyzed HCl oxidation reaction (Deacon reaction) [2–4]. One of the main challenges of CeO$_2$-based materials in automotive catalysts is to balance the oxygen supply in the exhaust gas stream between lean and rich operation of the engine by buffering and releasing oxygen, respectively. This oxygen exchange of CeO$_2$ is best described by the so-called "oxygen storage capacity" (OSC). To further improve thermal stability and the textural [5–7] as well as redox properties [8,9] of CeO$_2$-based materials without deteriorating the OSC, t-$Ce_{1-x}Zr_xO_2$ solid solutions are employed in automotive catalysis [10]. It has been demonstrated that $Ce_{1-x}Zr_xO_2$ solid solutions are also chemically much more stable against in-depth chlorination

than pure CeO$_2$ in the HCl oxidation. The solid solutions $Ce_{1-x}Zr_xO_2$ are shown to be both catalytically active and chemically stable over a wide concentration range of Ce from 20 at.-% to 80 at.-% [11,12]. Solid solutions $Ce_{1-x}Zr_xO_2$ are also used in other oxidation reactions [13].

In previous years, it was reported that the OSC can be dramatically enhanced by transforming a t-$Ce_{0.5}Zr_{0.5}O_2$ solid solution featuring a statistical distribution of Zr and Ce atoms into a crystalline structure possessing an ordered cation sublattice, the so-called "kappa phase" κ-$Ce_2Zr_2O_8$ [14–20]. The κ-$Ce_2Zr_2O_8$ phase contains an ordered array of cations, and 1/8 of the oxygen anions can readily be removed leading to an extraordinarily high OSC. The κ-$Ce_2Zr_2O_8$ phase has demonstrated high catalytic activity in the combustion of chlorinated compounds [21,22] due to the improved OSC properties.

In general, the κ-$Ce_2Zr_2O_8$ phase is synthesized starting from t-$Ce_{0.5}Zr_{0.5}O_2$ solid solution which is reduced by hydrogen at high temperatures to form the pyrochlore $Ce_2Zr_2O_7$ phase (pyr-$Ce_2Zr_2O_7$). In this way oxygen vacancies are generated, which facilitate the mobility of the cations and therefore the ordering of the cationic sublattice. The synthesis of κ-$Ce_2Zr_2O_8$ is achieved by a mild re-oxidation of pyr-$Ce_2Zr_2O_7$ at 600 °C under atmospheric conditions.

In literature most of the studies employed reduction temperatures of 1300 °C and below for the synthesis of the pyr-$Ce_2Zr_2O_7$ phase [17,23–28]. Hence, the single steps in the synthesis of κ-$Ce_2Zr_2O_8$ seem to be straightforward and well established. However, the reduction of t-$Ce_{0.5}Zr_{0.5}O_2$ at quite elevated temperatures represents a critical issue. In this contribution we will report on the synthesis of the κ-$Ce_2Zr_2O_8$ phase by varying the reduction temperature from 1300 °C to 1500 °C at which the t-$Ce_{0.5}Zr_{0.5}O_2$ solid solution is chemically reduced by hydrogen to form pyr-$Ce_2Zr_2O_7$. The structural evolution resulting in the pyrochlore and kappa phases (pyr-$Ce_2Zr_2O_7$ and κ-$Ce_2Zr_2O_8$, respectively) is subjected to in-depth characterization, employing a variety of different experimental techniques, including X-ray diffraction (XRD), X-ray absorption spectroscopy (XAS) and Raman spectroscopy. We show as a main outcome of these studies that reduction at 1300 °C is not sufficient to produce phase-pure pyr-$Ce_2Zr_2O_7$ and κ-$Ce_2Zr_2O_8$, rather reduction temperatures as high as 1500 °C are required.

2. Experimental

2.1. Synthesis

For the preparation of the t-$Ce_{0.5}Zr_{0.5}O_2$ solid solution, 2.5 mmol $Ce(NO_3)_3 \cdot 6H_2O$ and 2.5 mmol $ZrO(NO_3)_2 \cdot xH_2O$ were dissolved in 40 mL H_2O, using an ultrasonic bath (60 °C, 240 W power, 37 Hz) for 120 min and shaking it every 30 min to stir up the sediment. We added 30 ml of glacial acetic acid to the slightly opaque solution, and treated this solution in an ultrasonic bath (60 °C, 240 W power, 37 Hz) for 60 min. The solution was then heated in an open beaker at 130 °C for 24 h, resulting in a xerogel-like foam. After grinding the sample and heating up to 500 °C for 4 h (heating rate 3 K min^{-1} in air) in a ceramic crucible with a non-airtight cover, we obtained a faint yellow/white powder of t-$Ce_{0.5}Zr_{0.5}O_2$ (cf. Fig. 1, top left).

t-$Ce_{0.5}Zr_{0.5}O_2$ was then reduced by hydrogen at various high temperatures (1300, 1400, or 1500 °C). In this way oxygen vacancies were generated, which promoted the mobility of cations and thus the ordering of the cationic sublattice [17,23–26]. This ordering of the cationic sublattice has been visualized in a previous high resolution TEM (transmission electron microscopy) study employing atomic-resolved chemical mapping. [27] The resulting so-called pyrochlore phase pyr-$Ce_2Zr_2O_{7+\delta}$ was a black powder (cf. Fig. 1, top center). The synthesis of the κ-$Ce_2Zr_2O_8$ phase was based on a mild re-oxidation of pyrochlore phase $Ce_2Zr_2O_{7+\delta}$ at 600 °C under ambient atmosphere, yielding a yellow powder (cf. Fig. 1, top right). Using TEM it could be proven that the ordered cation arrangement is maintained after mild oxidation up to 600 °C [28]. In Fig. 1 the temperature protocol and the used composition of the reaction feeds are summarized.

The main drawback of this high temperature synthesis route (1500 °C) is the sintering of the material, resulting in an active surface area of below 1 m^2 g^{-1}. The SEM image (cf. Fig. 2) nicely shows that the grains possess sizes in the sub-micrometer range,
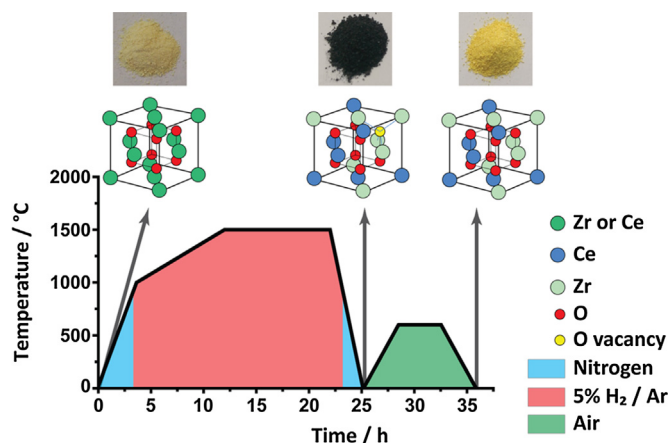

Fig. 1. Temperature profile and reaction conditions for the synthesis of the κ-$Ce_2Zr_2O_8$ phase. The starting material is a solid solution (almost white powder) t-$Ce_{0.5}Zr_{0.5}O_2$, possessing a statistical spatial distribution of Zr and Ce. High-temperature reduction at 1300, 1400, 1500 °C in 5% H_2/Ar (noxal) leads to black powder. Up to 800 °C heating was performed under nitrogen atmosphere and subsequently switched to noxal. As temperature ramp we used 4.5 K min^{-1} up to 1000 °C and subsequently a temperature ramp of 1 K min^{-1} was applied. The final temperature of either 1300, 1400, or 1500 °C was kept for 10 h before cooling the sample down to room temperature. The resulting pyrochlore phase is mildly re-oxidized at 600 °C in air for 4 h leading to the desired κ-$Ce_2Zr_2O_8$ phase. Shown are also the reduced unit cells of t-$Ce_{0.5}Zr_{0.5}O_2$, pyr-$Ce_{0.5}Zr_{0.5}O_2$ and κ-$Ce_2Zr_2O_8$. Actually, the unit cells of the pyrochlore and κ-$Ce_2Zr_2O_8$ are twice as large in all three directions compared to the tetragonal starting phase. The unit cells shown are adopted from Ref. [9].

thus being compatible with the small active surface area. At lower reduction temperatures of 1000 °C, the active surface area of the resulting κ-$Ce_2Zr_2O_8$ phase (not phase-pure as shown later) can be maintained to be 20–40 m^2 g^{-1} [29].

2.2. Characterization

2.2.1. X-ray diffraction

X-ray diffraction measurements were performed on a PANalytical Empyrean diffractometer with a Cu Kα X-ray source (1.54060 Å, Ni filter for filtering the Cu K$_\beta$-radiation). The Rietveld refinement of powder XRD patterns has been performed using the software FULLPROF. The modified Thompson-Cox-Hastings pseudo-Voigt method, which is known to allow for facile size analysis, was chosen as profile function. In this approach, we assumed that line broadening of the deconvoluted profile is a result of the small crystallite size and lattice microstrain. The values of the half-width parameters, V, W, and X, were kept constant at values determined by using LaB$_6$. The quality of the refinement was assessed by the values of the discrepancy factor (profile weighted residual error), R$_{wp}$, and the goodness-of-fit, χ^2.
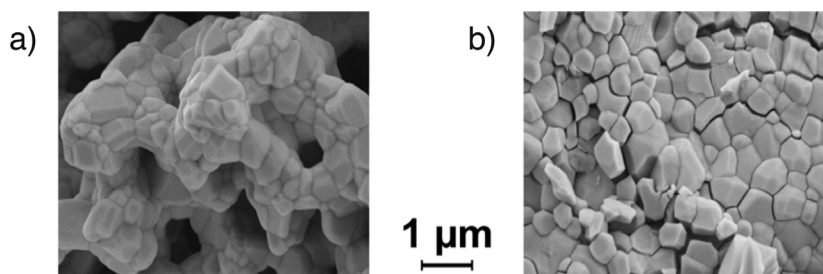

Fig. 2. Scanning electron microscopy (SEM) images of the pyrochlore phase pyr-$Ce_2Zr_2O_7$ (left) and the κ-$Ce_2Zr_2O_8$ phase (right) when the solid solution t-$Ce_{0.5}Zr_{0.5}O_2$, possessing a statistical spatial distribution of Zr and Ce is reduced at 1500 °C in 5% H_2/Ar (noxal).

2.2.2. Raman spectroscopy

A commercially available Renishaw inVia Raman microscope was used for the Raman measurements of all the samples. The spectra were taken using a 632.8 nm HeNe laser (10 mW) as excitation source and were recorded in a backscattering geometry at room temperature. The excitation laser was focused with a $50 \times$ objective onto the sample surface. The same objective was used to collect the scattered light, which was then dispersed by a spectrometer with a focal length of 250 mm and was finally detected by a charge-coupled device (CCD) camera with a spectral resolution of about $1\,cm^{-1}$.

2.2.3. X-ray absorption spectroscopy

The XAS measurements were performed at beamline BM 08 at European Synchrotron Radiation Facility (ESRF, Grenoble, France). A Si(311) double crystal monochromator was used for measurements at the Zr K-edge (17998 eV). The second monochromator crystal was tilted for optimal harmonic rejection. The spectra were recorded in transmission mode using ionisation chambers as detectors. Energy calibration was performed with a Zr metal foil. The solid samples were pressed into self-supporting pellets using cellulose as a binder.

Data evaluation started with background absorption removal from the experimental absorption spectrum by using the automated removal routine found in the Athena software [30]. The threshold energy E_0 was determined as the maximum in the first derivative spectrum. To determine the normalization function, corrected for pre-edge absorption, a piecewise polynomial was used. It was adjusted in such a way that the low-R components of the resulting Fourier transform were minimal. After division of the background-subtracted spectrum by its smooth part, the photon energy was converted to photoelectron wave numbers k. The resulting $\chi(k)$-function was weighted with k^2 and Fourier transformed using a Hanning window function. Data analysis was performed in k-space on unfiltered data in the region $3\text{–}16\,Å^{-1}$, using the Artemis software [30]. The amplitude reduction factor $S_0{}^2$ was calibrated against metallic zirconium and determined to be 0.9.

Coordination numbers (CNs) were kept fixed in the fittings, based on the data determined by the Rietveld refinement of XRD data. The threshold energy correction ΔE_0, the distances and the Debye-Waller factors were free to vary in all the fittings. The relative contributions of the crystalline phases were fixed to the amounts determined by Rietveld refinement.

3. Results and discussion

3.1. Transformation of t-$Ce_{0.5}Zr_{0.5}O_2$ solid solution to pyr-$Ce_2Zr_2O_7$ and κ-$Ce_2Zr_2O_8$

This chapter deals with the transformation of the $Ce_{0.5}Zr_{0.5}O_2$ solid solution into the pyrochlore phase by high-temperature reduction at 1500 °C in 5% H_2/Ar (noxal) atmosphere and the subsequent mild re-oxidation at 600 °C in ambient atmosphere to form the κ-$Ce_2Zr_2O_8$ phase. By combining X-ray diffraction (XRD) and X-ray absorption spectroscopy (XAS), the structural changes during this transformation were studied. Raman spectroscopy was applied to follow the changes in the vibrational properties and also to probe the phase purity based on the sensitivity of this method.

3.1.1. X-ray diffraction

XRD analysis reveals that the formed solid solution $Ce_{0.5}Zr_{0.5}O_2$ crystallizes in the tetragonal crystal system with an average crystallite size of 8 nm as deduced from the corresponding Rietveld refinement. Quite in contrast, the XRD pattern of the pyrochlore phase (1500 °C preparation) reveals quite sharp Bragg reflections
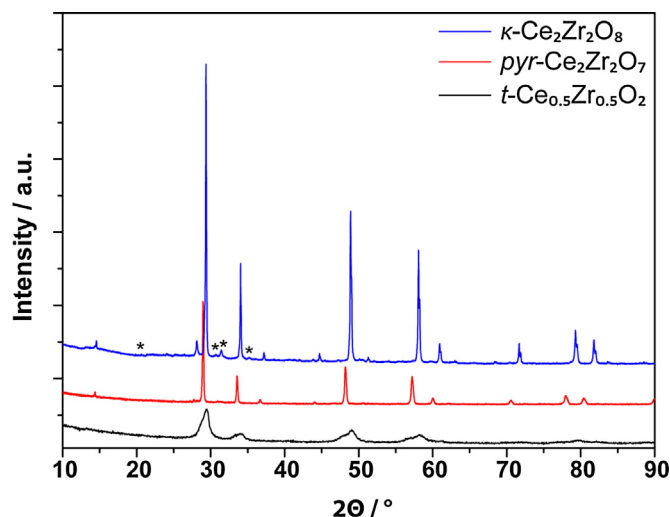

Fig. 3. XRD patterns of the t-$Ce_{0.5}Zr_{0.5}O_2$ in comparison with the pyrochlore phase and the κ-$Ce_2Zr_2O_8$ phase. For clarity the patterns are shifted vertically. The positions marked by asterisks are indicative of the κ-$Ce_2Zr_2O_8$ phase and forbidden in the space group of pyrochlore phase pyr-$Ce_2Zr_2O_7$.

corresponding to an average crystallite size of 78 nm (cf. Fig. 3). As expected, the high-temperature reduction leads to pronounced sintering of the particles. For comparison, the dominating XRD reflections of the t-$Ce_{0.5}Zr_{0.5}O_2$ are shifted to lower diffraction angles, which is attributed to an expansion of the unit cell. Obviously, the size variation of the unit cell due to the removal of oxide ions is overcompensated by the size increase of the Ce cation when switching the valence state from +4 (0.87 Å) to +3 (1.14 Å). For t-$Ce_{0.5}Zr_{0.5}O_2$ we obtained lattice constants of 5.35/3.73 Å, being identified as the t' phase of tetragonal crystal system with c/a ratio of 1.43. This result is in accordance with the proposed crystallography of the polymorphs in the CeO_2-ZrO_2 system [28]. The unit cell of the pyrochlore phase is cubic with dimensions doubled in all three directions due to ordering of the cationic sublattice (10.68 Å).

The XRD pattern becomes even more pronounced when the pyrochlore phase is mildly oxidized at 600 °C. Additional Bragg signals show up in the diffraction scan (in particular at small diffraction angles) which are indicative of the evolution of the κ-$Ce_2Zr_2O_8$ phase [12]. The average crystallite size (coherently diffracting domains) can be estimated to be 170 nm. In comparison to the pyrochlore structure pyr-$Ce_2Zr_2O_7$, the XRD reflections shift to higher diffraction angles so that the position of the dominant peaks matches with those of the tetragonal phase. The lattice constant of the cubic structure of κ-$Ce_2Zr_2O_8$ is determined to be 10.53 Å.

These results are in quantitative agreement with those of Kishimoto et al. [17,26]. Kishimoto reported a lattice constant of the pyrochlore phase pyr-$Ce_2Zr_2O_7$ of 10.75 Å, a little larger than our value, and a lattice constant of 10.53 Å for the κ-$Ce_2Zr_2O_8$ phase, in quantitative agreement with our investigation.

The structure of pyr-$Ce_2Zr_2O_7$ is described by a cubic system with a space group of Fd-3m, by an ordered arrangement of Ce^{3+} and Zr^{4+} ions along the <110> direction, and by the stable sixfold coordination of Zr^{4+} by six equivalent Zr—O bonds of about 2.17 Å in length. This atomic geometry of the pyrochlore phase agrees well with those previously published [10,17]. The structural details of the Rietveld analysis are compiled in Table 1.

The atomic structure of the κ-$Ce_2Zr_2O_8$ was also determined by a detailed Rietveld analysis. The crystallography of the κ-$Ce_2Zr_2O_8$ is described by the cubic system with the space group $P2_13$, in particular by the ordered arrangement of Ce^{4+} and Zr^{4+} ions and the "unstable" eightfold coordination of Zr^{4+}. Two inequivalent ZrO_8
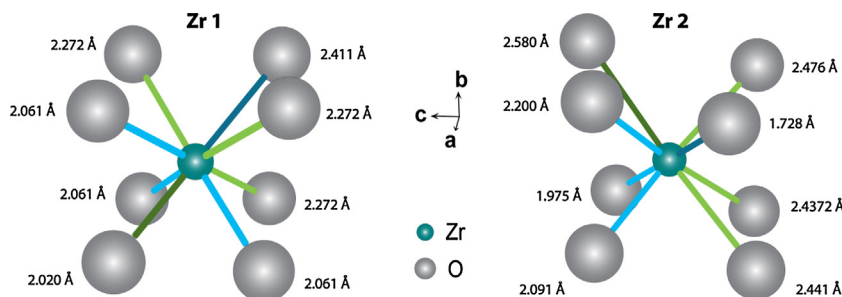
Fig. 4. The atomic geometry of the two non-equivalent ZrO_8 polyhedra in the κ-$Ce_2Zr_2O_8$ phase.

Table 1
Rietveld analysis of pyrochlore phase *pyr*-$Ce_2Zr_2O_7$ which was prepared by chemical reduction of the $Ce_{0.5}Zr_{0.5}O_2$ solid solution with 5% H_2/Ar (noxal) at 1500 °C. R_{wp} is the reliability factor, and U the isotropic temperature factor. χ^2 measures the quality of the fit.

Space group: $Fd\bar{3}m$
Lattice constant a/Å: 10.6765(2)
Unit cell volume/Å³: 1216.99(2)
R_{wp} (%): 14.4; χ^2: 0.193

atom	site	occupancy	x	y	z	U (Å²)
Ce	16c	1	0	0	0	0.0037(1)
Zr	16d	1	0.5	0.5	0.5	0.0064(1)
O1	48f	1	0.3988(9)	0.1250	0.1250	
O2	8a	0.912(5)	0.1250	0.1250	0.1250	0.00022(2)
O3	8b	0.088(5)	0.3750	0.3750	0.3750	

polyhedrons are formed, as illustrated in Fig. 4. The Zr—O bond lengths vary quite remarkably from 1.72 Å to 2.58 Å in one of the ZrO_8 polyhedra with eight non-equivalent Zr—O bonds, while the other ZrO_8 polyhedra can be envisioned as consisting of two distorted tetrahedrons T_1 and T_2 with one short (2.03 Å (T_1), 2.06 Å (T_2)) and three long Zr—O bonds (2.27 Å (T_1), 2.42 Å (T_2)). The oxygen atoms which can be removed from the κ-$Ce_2Zr_2O_8$ phase during chemical reduction by hydrogen form two tetrahedra, featuring an averaged Zr—O bond length of 2.27 Å that is slightly longer than the other Zr—O bonds ranging from 2.15 Å to 2.22 Å. This finding is compatible with a weaker Zr—O bond and therefore a facilitated release of oxygen. A previous TEM study [27] consistent with a theoretical study [31] indicated that the symmetry of κ-$Ce_2Zr_2O_8$ is Fd-3m rather than $P2_13$. However, Rietveld analysis using a symmetry of Fd-3m for κ-$Ce_2Zr_2O_8$ is not able to fit the XRD data consistent with a recent density functional theory study [32].

These ZrO_8 configurations of κ-$Ce_2Zr_2O_8$ are largely consistent with two sets of distorted tetrahedral configurations as suggested previously on the basis of an Extended X-ray Absorption Fine Structure (EXAFS) analysis for the cubic-ZrO_2 phase in comparison with tetragonal-ZrO_2 [33]. This important structural detail of κ-$Ce_2Zr_2O_8$ will help us in the interpretation of the X-ray Absorption Near-Edge Spectroscopy (XANES) data discussed in Section 3.1.3. The structural details of the Rietveld analysis are in remarkable agreement with those obtained by Kishimoto et al. [17] and are collected in Table 2. It is important to note that the present study goes beyond these previous studies in that we address the dependence of the formation of the κ-$Ce_2Zr_2O_8$ structure on the high-temperature treatment in the reduction step and are thus able to optimize the synthetic procedure.

3.1.2. Raman spectroscopy

In Fig. 5 we compare the Raman spectra of the $Ce_{0.5}Zr_{0.5}O_2$ solid solution with those of the pyrochlore phase and the κ-$Ce_2Zr_2O_8$ phase. The solid solution $Ce_{0.5}Zr_{0.5}O_2$ is of tetragonal structure. For the tetragonal symmetry of space group $P4_{2/nmc}$ (D_{4h}), there are six
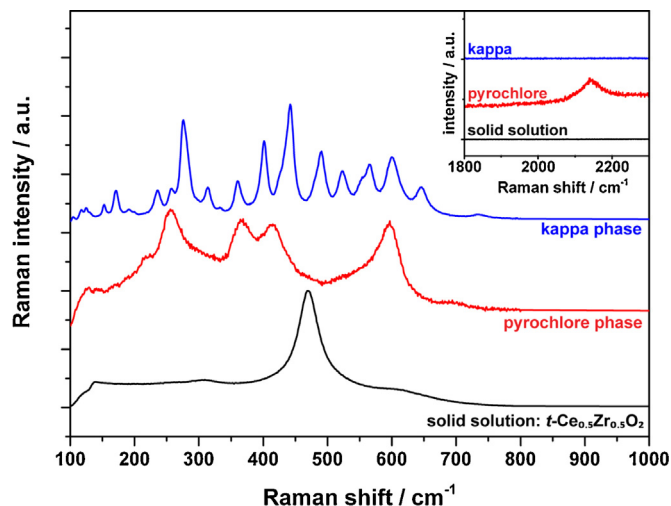

Fig. 5. Raman spectra of the solid solution *t*-$Ce_{0.5}Zr_{0.5}O_2$ in comparison with the pyrochlore phase and the κ-$Ce_2Zr_2O_8$ phase. The inset shows an additional band at 2140 cm⁻¹ for the pyrochlore phase, not visible in the mixed oxide or κ-$Ce_2Zr_2O_8$. For clarity the spectra are shifted vertically.
In case of the ideal *pyr*-$Ce_2Zr_2O_7$ all the Ce atoms should have oxidation number +3 whereas in the solid solution *t*-$Ce_{0.5}Zr_{0.5}O_2$ as well as in the ideal κ-$Ce_2Zr_2O_8$ its oxidation number should be +4. It should be noted that Ce^{3+} shows a characteristic electronic Raman scattering signal at about 2100 cm⁻¹ which arises due to a spin-flip of the electron in the inner f-shell between the levels $^2F_{7/2}$ and $^2F_{5/2}$ [45,46] and is not observed for Ce^{4+}. The inset shows corresponding spectra of the three samples demonstrating that indeed Ce^{3+} is present in the pyrochlore phase and not detectable in the other two phases.

Raman-allowed modes (A_{1g}, $2B_{1g}$, $3E_g$) expected. In the cubic case (space group $Fm3m$ (O_h)), there would be only one Raman-allowed mode, the triply degenerate F_{2g} mode which in cubic CeO_2 is located at 463 cm⁻¹. Our Raman spectrum of the $Ce_{0.5}Zr_{0.5}O_2$ solid solution is somewhat simpler than the tetragonal case consisting of one dominating signal at 473 cm⁻¹ with two broader shoulders at about 300 cm⁻¹ and 630 cm⁻¹. It indicates that the $Ce_{0.5}Zr_{0.5}O_2$ solid solution has almost a cubic structure.

The Raman spectrum of the solid solution $Ce_{0.5}Zr_{0.5}O_2$ is in accordance with other reports in the literature [34–36]. When the solid solution is chemically reduced at 1500 °C by hydrogen, the pyrochlore phase is obtained. The space group of the ideal *pyr*-$Ce_2Zr_2O_7$ is Fd-3m (O_h) with two molecular units in the primitive unit cell. The corresponding factor analysis yields six Raman-active modes (A_{1g}, E_g, $4F_{2g}$) [37,38]. Five strong Raman features are present at about 600, 400, 350, 250, and 220 cm⁻¹. In addition, there is a shoulder at 550 cm⁻¹. Thus, the number of Raman signals is in accordance with the factor analysis. This kind of spectrum is typical of pyrochlore oxides [36,38]. As discussed in Section 3.1.1, the reflections in XRD patterns of the pyrochlore phase are much narrower than in the solid solution *t*-$Ce_{0.5}Zr_{0.5}O_2$. In contrast, the Raman signals of the pyrochlore phase are broader than those in the

Table 2

Rietveld analysis of the κ-Ce$_2$Zr$_2$O$_8$ phase which was prepared by chemical reduction of the t-Ce$_{0.5}$Zr$_{0.5}$O$_2$ solid solution in 5% H$_2$/Ar (noxal) at 1500 °C and mildly re-oxidized at 600 °C in air. R$_{wp}$ is the reliability factor, and U the isotropic temperature factor. χ^2 measures the quality of the fit.

Space group: $P2_13$
Lattice constant a/Å: 10.5266(3)
Unit cell volume/Å^3: 1166.45(2)
R_{wp} (%): 15.2
χ^2: 0.187

atom	site	occupancy	X	y	Z	U (Å^2)
Ce	4a	1	0.1321(4)	0.1321(4)	0.1321(4)	0.012(1)
Ce	12b	1	0.1210(5)	0.3694(5)	0.3734(5)	0.012(1)
Zr	4a	1	0.6297(4)	0.6297(4)	0.6297(4)	0.018(1)
Zr	12b	1	0.6239(5)	0.8700(5)	0.8760(6)	0.018(1)
O1	4a	0.9304(4)	0.0186(5)	0.0186(5)	0.0186(5)	
O2	4a	1	0.2520(5)	0.2520(5)	0.2520(5)	
O3	4a	0.8414(4)	0.5188(4)	0.5188(4)	0.5188(4)	
O4	4a	1	0.7626(4)	0.7626(4)	0.7626(4)	0.00302(2)
O5	12b	1	0.2466(6)	0.2609(5)	−0.0112(5)	
O6	12b	1	0.2079(6)	0.2206(6)	0.5272(6)	
O7	12b	1	0.0100(5)	−0.0200(6)	0.2607(5)	
O8	12b	1	0.0183(6)	0.0158(6)	0.7414(8)	

spectrum of the solid solution. The reason is that the XRD analysis is insensitive to the positions of the oxygen ions. The main features of the XRD pattern of pyrochlore are determined by the cation sublattice and thus indicative for the cation ordering, but less so for the occupation of oxygen sublattice. In contrast, all the Raman-active mode patterns involve displacement of the oxygen ions [39] and are thus sensitive to the oxygen sublattice occupation. The rather broad Raman signals of the pyrochlore phase suggest that there is still a significant degree of disorder on the oxygen sublattice. It cannot be assessed whether it arises from disorder of the oxygen vacancies (i.e. not all of them on Wyckoff position 8b of the fluorite-like structure) or from non-stoichiometry (i.e. δ ≠ 0 in Ce$_2$Zr$_2$O$_{7+δ}$). This is also in concordance with the finding that our Raman spectra of pyr-Ce$_2$Zr$_2$O$_{7+δ}$ differ slightly for different positions on the same sample (probably because of different grain sizes) as well as for the three different reduction temperatures (see Section 3.2.2).

When the pyrochlore phase pyr-Ce$_2$Zr$_2$O$_7$ transforms into the κ-Ce$_2$Zr$_2$O$_8$ phase by mild oxidation at 600 °C, the Raman spectrum changes dramatically, revealing more than 20 sharp modes. The narrow linewidths of the Raman features are indicative for a high degree of ordering, i. e. the oxidation has removed all the disorder from the oxygen sublattice. The large number of Raman active modes originates from the lower symmetry of the kappa phase (space group $P2_13$) compared with pyr-Ce$_2$Zr$_2$O$_7$ and the large primitive unit cell containing eight molecular units. A corresponding factor analysis yields 144 Raman active modes (24A, 24 E$_1$, 24E$_2$, 72F), i.e. many more than those observed. It is not possible to spectrally resolve all the modes, not even at low temperatures. The large number of modes falls into a narrow spectral window as anticipated for such a large unit cell containing only a few different atomic species. Thus, the modes are close in frequency. This fact in conjunction with the presence of residual disorder leads to a broadening of the modes which is larger than the spectral separation of the modes, i.e. many modes overlap and cannot be resolved. Our Raman spectrum of the κ-Ce$_2$Zr$_2$O$_8$ phase also agrees well with those published in the literature [16,25,40–44]. The presented Raman spectrum of κ-Ce$_2$Zr$_2$O$_8$ is consistent with a P2$_1$3 symmetry.

3.1.3. X-ray absorption spectroscopy

In Fig. 6 we compare the XANES spectra measured at the Zr K-edge of the t-Ce$_{0.5}$Zr$_{0.5}$O$_2$ solid solution with those of the pyrochlore phase and the κ-Ce$_2$Zr$_2$O$_8$ phase prepared at 1500 °C. The pre-edge absorption region around 18005 eV (labelled A) represents a transition to an empty bound state, in the case of Zr arising from a 1 s → 4d transition. This transition is influenced by
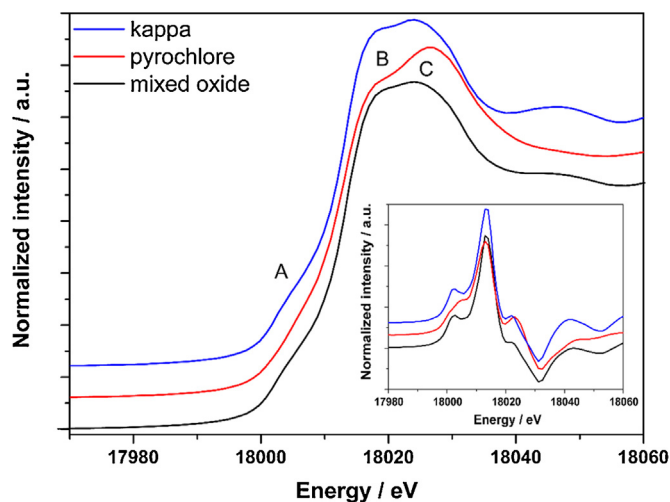

Fig. 6. XANES spectra at Zr K-edge of the solid solution t-Ce$_{0.5}$Zr$_{0.5}$O$_2$ in comparison with the pyrochlore phase and the κ-Ce$_2$Zr$_2$O$_8$ phase. In the inset the first derivative of these spectra is shown. For clarity the spectra are shifted vertically.

the degree of mixing of d and p orbitals (dipole selection rule: $\Delta l = +1$), and is enhanced by the tetrahedral geometry that allows more d-p mixing than in sevenfold coordination [34]. In the case of our samples, this pre-edge feature is not particularly evident in the XANES spectra, but this subtle feature is highlighted in the first derivative (inset of Fig. 6). According to Fig. 6, the pre-edges of the solid solution and the κ-Ce$_2$Zr$_2$O$_8$ phase are similarly pronounced, meaning that the local symmetry of Zr is very much alike. Quite in contrast, the pyrochlore phase reveals only a weakly developed pre-edge that is consistent with the development of a more symmetric environment, thus possibly hinting to cubic coordination.

These spectra can be compared to those of mixed Y$_2$O$_3$ and ZrO$_2$ solid solutions where the concentration of Y$_2$O$_3$ and therefore the concentration of oxygen vacancies is increased [34]. For low Y$_2$O$_3$ concentration, ZrO$_2$ exists in the tetragonal phase, revealing a pronounced pre-edge shoulder. With increasing Y$_2$O$_3$ concentration the pre-edge disappears which is indicative of Zr existing in a highly symmetric coordination [33]. In conclusion, the pre-edge structure is very sensitive to the symmetry of the Zr—O polyhedron, in agreement with mixed Ce-Zr-oxide systems.

The spectrum of the starting solid solution t-Ce$_{0.5}$Zr$_{0.5}$O$_2$, as expected, looks very similar to that of the Y-doped tetragonal ZrO$_2$ where the eightfold O coordination shell around the Zr-atom

Table 3
Microstructural parameters of the pyrochlore phase prepared at different reduction temperatures.

Sample (heating temperature°C)	Main phase-Pyrochlore			Minor phases	
	Fract. (wt%)	Average crystallite size/nm	Average microstrain ($\times 10^{-4}$)	Fract. (wt%)	Average crystallite size/nm
1300	44	37	51	56 (c-$Ce_{0.5}Zr_{0.5}O_2$)	21.4
1400	100	66	20.9	0	–
1500	100	78	25.5	0	–

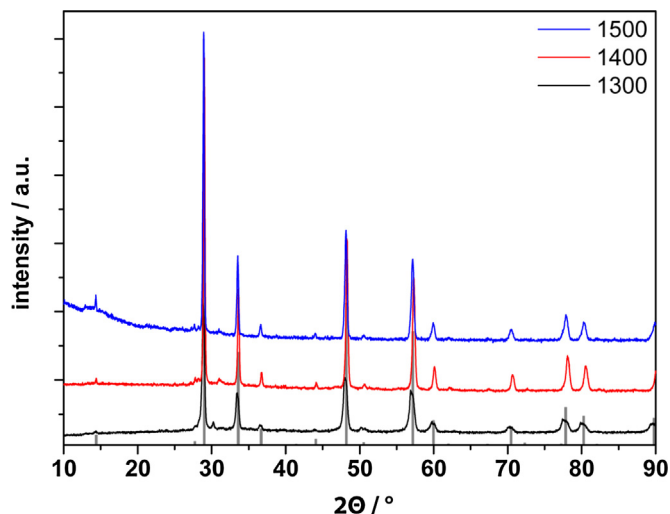**Fig. 7.** XRD data of the *pyr*-$Ce_2Zr_2O_7$ prepared at three reduction temperatures (values in °C) starting from a solid solution $Ce_{0.5}Zr_{0.5}O_2$. For clarity the XRD patterns are shifted vertically. Reflections according to JCPDS cards No. 16-8600 are included.

decomposes in two sets of non-equivalent Zr—O tetrahedra with Zr—O of 2.10 Å and 2.33 Å, respectively [34].

The second pronounced feature in the XANES spectra of Fig. 6 is the splitting of the main peak around 18020 eV (features B and C). Again the splitting feature of the κ-$Ce_2Zr_2O_8$ phase and that of the solid solution are very similar, while the pyrochlore phase is again distinctly different, showing a more pronounced splitting and an asymmetric intensity ratio in the doublet feature. Feature C is indeed correlated to the symmetry of the Zr—O local coordination, and its increased intensity in the pyrochlore phase indicates a more centrosymmetric site. The XANES spectrum of the pyrochlore phase compares well with that of the 20 mol% of Y_2O_3 in ZrO_2 solid solution, again being indicative of cubic symmetry in the Zr coordination shell. The XANES spectra κ-$Ce_2Zr_2O_8$, on the other hand, show both an increase in the intensity of feature A and a decrease in feature C, both aspects indicative of the expected decrease in symmetry.

3.2. Pyrochlore phase prepared at different reduction temperatures 1300, 1400, and 1500 °C

In order to optimize the preparation of phase-pure κ-$Ce_2Zr_2O_8$, we prepared the pyrochlore phase by chemical reduction by hydrogen at three different temperatures, namely 1300, 1400, and 1500 °C. In literature, the highest reduction temperature for preparing *pyr*-$Ce_2Zr_2O_7$ reported so far was 1300 °C [17,23–28]. Therefore, the temperatures used in this work can contribute to gain a better insight into the structural evolution of these mixed phases at higher temperatures.

3.2.1. X-ray diffraction data
In Fig. 7 we show the XRD data of *pyr*-$Ce_2Zr_2O_7$ prepared at three different reduction temperatures: 1300 °C, 1400 °C and 1500 °C. For

the sample treated at 1300 °C the XRD maxima are quite broad, indicating an average crystallite size of about 37 nm.

The pyrochlore phase (1300 °C) is only hardly detected, as the (111) reflection is only faintly visible. From the Bragg positions the lattice constant of the cubic structure is inferred to be 10.6728(4) Å. The specimen is not phase-pure, consisting of 44% *pyr*-$Ce_2Zr_2O_7$ and 56% cubic *c*-$Ce_{0.5}Zr_{0.5}O_2$.

The XRD pattern of the sample treated at 1400 °C displays much sharper reflections that are explained by a larger average crystallite size, amounting to 66 nm. Higher reduction temperatures facilitate sintering of the particles. The lattice constant turned out to be 10.6639(2) Å implying a slight contraction if compared to the treatment performed at 1300 °C. In this case (1400 °C), the compound is nearly phase-pure (cf. Table 3).

Increasing the preparation temperature to 1500 °C results in even sharper XRD reflections. The positions in the corresponding XRD 2θ scans are virtually preserved compared to the treatment at 1400 °C corresponding to a lattice constant of 10.6765(2) Å. The average crystallite size is calculated to be 78 nm.

3.2.2. Raman spectroscopy data
In Fig. 8 we show the Raman spectra of *pyr*-$Ce_2Zr_2O_7$ for various processing temperatures of 1300 °C, 1400 °C and 1500 °C. The spectra of the samples processed at 1400 °C and 1500 °C exhibit the same number of main Raman signals and this number is in accordance with the expectations, although the peak positions as well as the intensity ratios vary to some degree. However, a strong dependence of the Raman frequencies on stoichiometry is also observed for other pyrochlore oxides [36]. We believe that the variation of the spectra between the samples processed at 1400–1500 °C and within the corresponding batches is mainly due to different degrees of disorder on the anion lattice whereas the cation lattice is almost perfectly ordered. This behavior probably also reflects the symmetry of the pyrochlore structure being rather robust against variation of the x-coordinate of O1 (Wyckoff position 48f) in Table 1 [37]. Such disorder on the oxygen sublattice may partly explain the discrepancies between the Raman spectra of *pyr*-$Ce_2Zr_2O_7$ reported in the literature [16,25,40]. The considerable fraction of 56% of c-$Ce_{0.5}Zr_{0.5}O_2$ detected in the XRD analysis of the spectrum of the sample processed at 1400 °C leads to the additional feature in the Raman spectrum at about 470 cm^{-1}, which is the dominant signal in the Raman spectrum of c-$Ce_{0.5}Zr_{0.5}O_2$ and t-$Ce_{0.5}Zr_{0.5}O_2$ mixed phase [11]. The signal strength of this additional feature also somewhat implies that the Raman cross sections of the main signals of the pyrochlore phase and of the c-Ce0.5Zr0.5O2 are comparable in magnitude.

However, such a feature is observed in the spectrum of the sample processed at 1300 °C where the XRD analysis yields an admixture of 56% of this alloy to the pyrochlore phase. This somewhat implies that the Raman cross sections of the main signals of the pyrochlore phase and of the c-$Ce_{0.5}Zr_{0.5}O_2$ are comparable in magnitude.

3.2.3. X-ray absorption spectroscopy
In Fig. 9 we show the XANES spectra of *pyr*-$Ce_2Zr_2O_7$ for 1300 °C, 1400 °C and 1500 °C preparation. The first derivatives of these spectra are shown in the inset in order to highlight some of the most
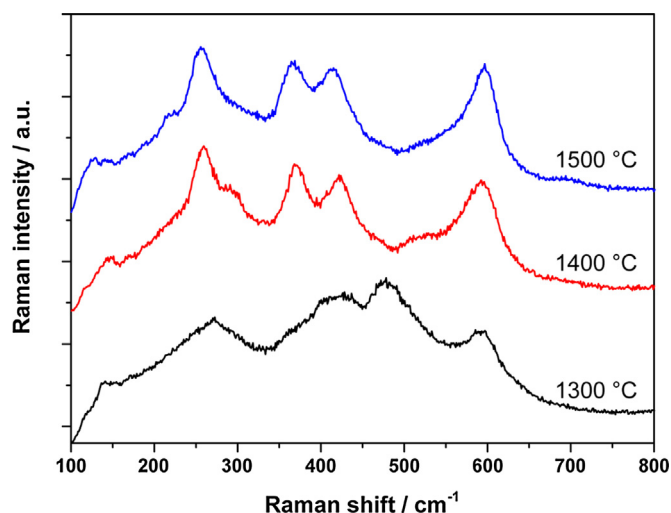
Fig. 8. Raman spectra of the *pyr*-$Ce_2Zr_2O_7$ prepared at three reduction temperatures starting from a solid solution t-$Ce_{0.5}Zr_{0.5}O_2$. For clarity the spectra are shifted vertically.
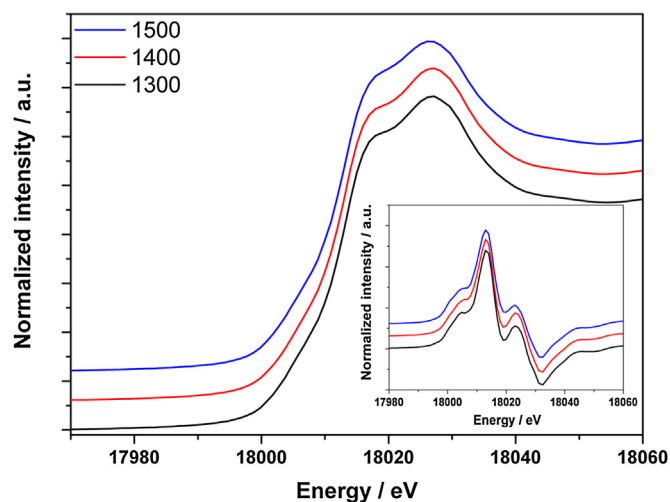

Fig. 9. XANES spectra at Zr K-edge of the pyrochlore phase prepared at three temperatures (1300 °C, 1400 °C, 1500 °C) in reducing atmosphere. In the inset the first derivative of these spectra is shown. For clarity the spectra are shifted vertically.

relevant features. The spectra look quite similar, although some subtle differences are apparent as well. The pre-edges in the three spectra are virtually identical, thus indicating a high local symmetry of the Zr cation presumably with cubic symmetry, common to both *pyr*-$Ce_2Zr_2O_7$ and c-$Ce_{0.5}Zr_{0.5}O_2$. Therefore, from these XANES data a clear decision which of the reduction temperatures results

in the structurally best ordered and phase-pure pyrochlore phase cannot be drawn.

The experimental EXAFS curves of the reduced samples are, as expected, quite diverse from that corresponding to the starting solid solution, while being very similar to each other. The spectrum of the sample reduced at 1500 °C shows a slight decrease in intensity in the range 9–13 Å^{-1}. The experimental EXAFS data of

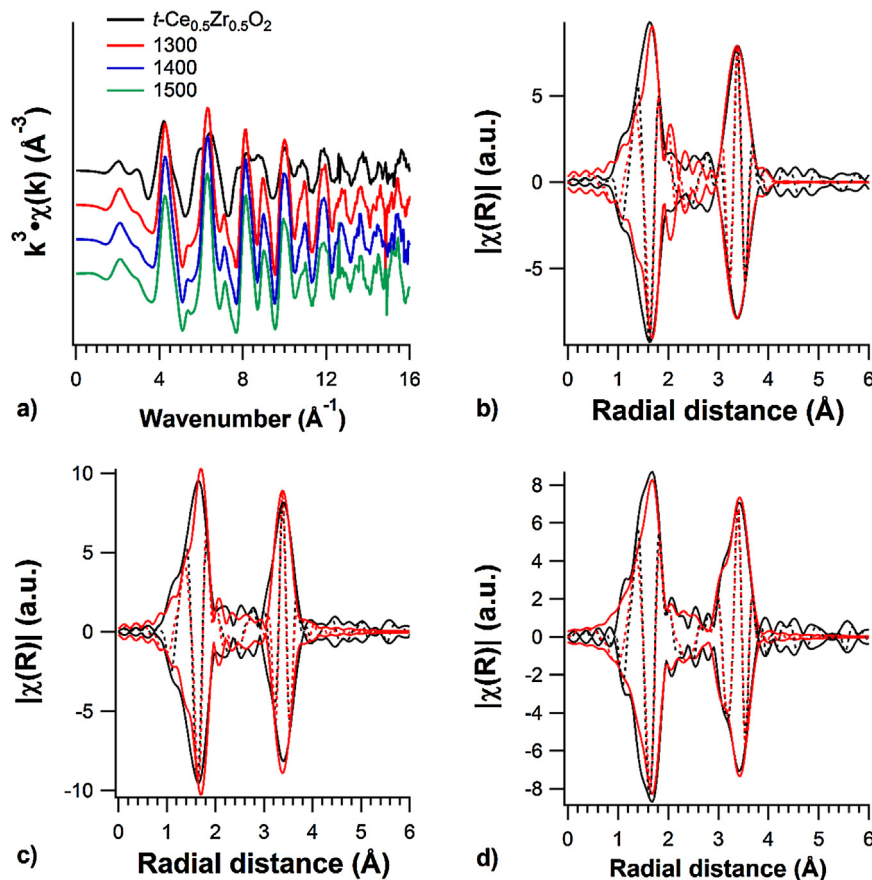**Fig. 10.** (a) k^3-weighted EXAFS function and Fourier Transforms with corresponding imaginary parts for pyrochlore samples at b) 1300 °C, (c) 1400 °C and (d) 1500 °C (black: experimental; red: fit; continuous lines: magnitude; dotted lines: imaginary. Data are not phase-corrected). (For interpretation of the references to colour in this figure legend, the reader is referred to the web version of this article.)
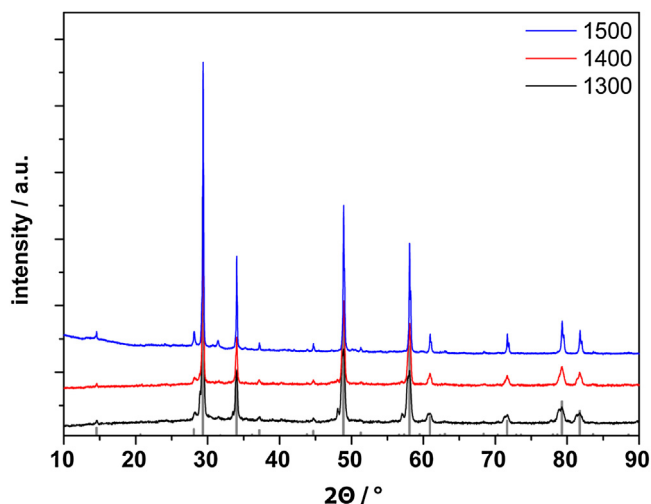
Fig. 11. XRD data of the κ-Ce$_2$Zr$_2$O$_8$ phase starting from *pyr*-Ce$_2$Zr$_2$O$_7$ prepared at three different reduction temperatures 1300 °C, 1400 °C, and 1500 °C. Reflections according to JCPDS cards No. 90-465 are included. For clarity the spectra are shifted vertically.

Fig. 12. Raman spectra of the of the κ-Ce$_2$Zr$_2$O$_8$ phase prepared at two reduction temperatures (1300 °C, 1500 °C) starting from a solid solution t-Ce$_{0.5}$Zr$_{0.5}$O$_2$. For clarity the spectra are shifted vertically.

the three pyrochlore samples were analyzed, in the 3–16 Å^{-1} interval (Fig. 10). The three Fourier transforms (FTs) are very similar presenting, after phase-correction, a first maximum at about 2.1 Å, corresponding to the Zr—O distance, and a second one at about 3.8 Å, indicative of the Zr—Ce and Zr—Zr bonds. The decrease in intensity at high *k* values in the 1500 °C samples appears, in the FT, as a slight second shell splitting.

The results of the fittings are compiled in Table 4 and presented in Fig. 10 (showing both the magnitude and the imaginary part of the FTs). For the pyrochlore structure, the Zr—O2 width represents the distance between the absorber and the oxygen vacancies, with partial occupancy expressed in parenthesis. With increasing temperature there is an expansion of the pyrochlore structure, resulting in a lengthening of the Zr-scatterers distances. With increasing temperature, the aforementioned splitting in the second shell appears, and indeed the fitting of samples reduced at 1400 and especially 1500 °C reveals a slight distortion in the Ce-Zr shell, with Zr atoms moving slightly closer to the scatterer.

The quite high values for the disorder-related Debye-Waller factor suggest that the pyrochlore lattice is characterized by a highly disordered local Zr—O bond situation [9], as also evidenced by Raman measurements (Section 3.2.2).

3.3. Preparation of the κ-Ce$_2$Zr$_2$O$_8$ starting from differently prepared pyrochlore phases

The κ-Ce$_2$Zr$_2$O$_8$ phase was prepared by mild re-oxidation at 600 °C in air of the differently prepared *pyr*-Ce$_2$Zr$_2$O$_7$ phases (1300, 1400, 1500 °C). The full structural characterization includes XRD, Raman and X-ray absorption experiments. We assume that the cationic lattice does not alter upon mild oxidation at 600 °C, consistent with recent TEM experiments [28].

3.3.1. X-ray diffraction data
In Fig. 11 we summarize the XRD measurements of the κ-Ce$_2$Zr$_2$O$_8$ phases starting from *pyr*-Ce$_2$Zr$_2$O$_7$ prepared at three different reduction temperatures (1300, 1400, and 1500 °C). The main reflections for all three samples are located at very similar positions consistent with the lattice constants being practically identical, namely 10.53 Å, 10.52 Å, and 10.52 Å, respectively. Except for the 1500 °C preparation, the samples are not phase-pure (cf. Table 5) as expected from the corresponding *pyr*-Ce$_2$Zr$_2$O$_7$ phases.
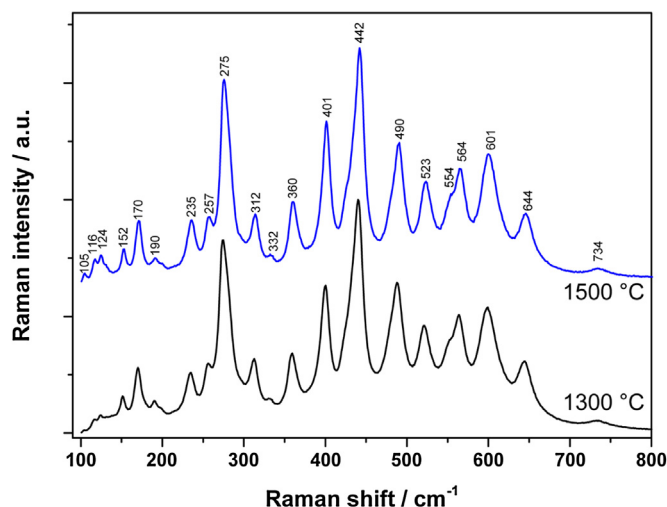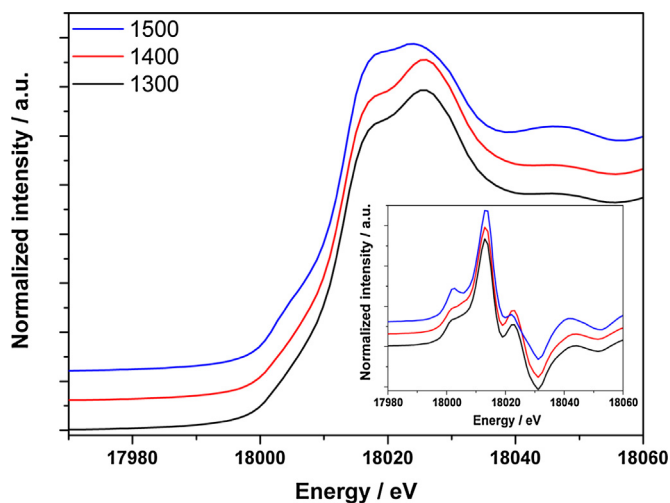

Fig. 13. XANES spectra at the Zr K-edge of the κ-Ce$_2$Zr$_2$O$_8$ phases prepared by mild re-oxidation at 600 °C of the differently prepared pyrochlore phases (1300 °C, 1400 °C, 1500 °C). In the inset the first derivative of these spectra is shown. For clarity the spectra are shifted vertically.

From the FWHM of the most intense reflection the mean crystallite size can be inferred (cf. Table 5). The mean crystallite size for the 1300 °C and 1400 °C specimen is almost identical to those found for the respective pyrochlore phases. This finding is reasonable, as the oxidation temperature is 600 °C, far below the preparation temperature of the pyrochlore phases (>1300 °C). Therefore, no further sintering is expected to occur. The 1300 °C specimen is not phase-pure containing 44.8% κ-Ce$_2$Zr$_2$O$_8$, 52.5% c-Ce$_{0.5}$Zr$_{0.5}$O$_2$, and 2.7% t-Ce$_{0.5}$Zr$_{0.5}$O$_2$ but also the 1400 °C sample is not phase-pure as it contains 3.4% of cubic c-Ce$_{0.5}$Zr$_{0.5}$O$_2$ besides the κ-Ce$_2$Zr$_2$O$_8$ phase. The tetragonal phase is clearly identified by an additional diffraction peak at around 48° (cf. Fig. S1), so that the corresponding concentrations could be determined with high accuracy.

However, the average crystallite size of the 1500 °C specimen increases from 78 nm for the *pyr*-Ce$_2$Zr$_2$O$_7$ to 167 nm for the κ-Ce$_2$Zr$_2$O$_8$. Since this effect cannot be traced to a pure microstrain effect, we surmise that antiphase boundaries may heal during the mild oxidation process thus increasing the average crystallite size (coherently diffracting domains). We emphasize that only the preparation at 1500 °C leads to a phase-pure κ-Ce$_2$Zr$_2$O$_8$ phase.

Table 4
Fitting of EXAFS data of the reduced samples prepared at 1300, 1400, and 1500 °C. The coordination number for the Zr—O2 distance was free to vary, in order to determine the occupancy of the oxygen vacancies.

Sample	Crystallographic phase	Neighbor	Coord. number	Distance (Å)	Debye-Waller factor σ^2 (10^{-3} Å^2)
OR_1300	Pyrochlore ($\Delta E_0 = -5.2 \pm 2.1$)	O1	6	2.11 ± 0.01	2.9 ± 2.1
		O2	2 (0.0)	2.27 ± 0.01	2.9 ± 2.1
		Ce1	6	3.81 ± 0.01	4.7 ± 3.4
		Zr1	6	3.81 ± 0.01	3.2 ± 2.1
	Cubic ($\Delta E_0 = -3.6 \pm 1.9$)	O1	8	2.19 ± 0.02	2.9 ± 2.1
		Zr1	6	3.92 ± 0.01	3.2 ± 2.1
		Ce1	6	3.92 ± 0.01	4.7 ± 3.4
OR_1400	Pyrochlore ($\Delta E_0 = -3.5 \pm 1.6$)	O1	6	2.14 ± 0.02	2.9 ± 1.1
		O2	2 (0.6)	2.27 ± 0.02	2.9 ± 1.1
		Ce1	6	3.73 ± 0.02	4.7 ± 3.4
		Zr1	6	3.67 ± 0.02	3.2 ± 2.1
OR_1500	Pyrochlore ($\Delta E_0 = -2.4 \pm 1.8$)	O1	6	2.14 ± 0.02	5.4 ± 1.1
		O2	2 (0.2)	2.28 ± 0.02	5.4 ± 1.1
		Ce1	6	3.73 ± 0.02	6.5 ± 1.3
		Zr1	6	3.65 ± 0.03	10.1 ± 2.3

Table 5
Structural parameters of κ-$Ce_2Zr_2O_8$ phase prepared at different temperatures.

	Phase 1-kappa		Phase 2 and/or (Phase 3)	
Sample	Fract (%)	Average crystallite size/nm	Fract. (%)	Average crystallite size/nm
1300	44.8	40.8	52.5 (c-$Ce_{0.5}Zr_{0.5}O_2$) 2.7 (t-$Ce_{0.5}Zr_{0.5}O_2$)	27.4 79.9
1400	96.6	56.6	3.4 (c-$Ce_{0.5}Zr_{0.5}O_2$)	62.4
1500	100	166.5	–	–

Taking into account the similarities of the XRD patterns of the relevant structures (κ-$Ce_2Zr_2O_8$, the cubic Fm3m structure c-$Ce_{0.5}Zr_{0.5}O_2$ and pyr-$Ce_2Zr_2O_7$), it is helpful to compare the theoretical XRD patterns of these three structures assuming structural parameters being analogous to those used for the Rietveld refinement. It is seen (Fig. S2) that κ-$Ce_2Zr_2O_8$ substantially differs from the other two structures, so that κ-$Ce_2Zr_2O_8$-in principle-can be well identified even in mixtures of these three structures. Furthermore, pyr-$Ce_2Zr_2O_7$ shows reflections being absent for the cubic c-$Ce_{0.5}Zr_{0.5}O_2$ structure. Indeed our XRD experiments present reflections (e.g. at 2θ = 31.7°) which are only present for κ-$Ce_2Zr_2O_8$ and therefore allow for a meaningful and accurate quantification of the composition of the mixtures using the Rietveld refinement.

3.3.2. Raman spectroscopy data

In Fig. 12 we show the Raman spectra of the κ-$Ce_2Zr_2O_8$ phase prepared at two different reduction temperatures, namely 1300 °C and 1500 °C. Despite the significant variations in the Raman spectra of the corresponding pyrochlore phases, the Raman spectra of the κ-$Ce_2Zr_2O_8$ phase are virtually identical. In particular, it should be noted that, although the 1300 °C sample is a mixture of 44% κ-$Ce_2Zr_2O_8$ and 56% of c-$Ce_{0.5}Zr_{0.5}O_2$ according to the XRD analysis, the main Raman feature of c-$Ce_{0.5}Zr_{0.5}O_2$ at 470 cm^{-1} cannot be distinguished in the spectrum of the 1500 °C sample. This is surprising at first sight, however, it is explained by the fact that the Raman cross sections of the signals of κ-$Ce_2Zr_2O_8$ are at least one order of magnitude larger than those of pyr-$Ce_2Zr_2O_7$ and of the c-$Ce_{0.5}Zr_{0.5}O_2$ alloy. Therefore, both spectra basically look like the spectrum indicative for the κ-phase as reported in the literature [16,25,40–44]. Furthermore, the oxidation process removes the disorder on the oxygen sublattice of κ-$Ce_2Zr_2O_8$ yielding very sharp spectral features. The finding is in accordance with an ordered cation sublattice in the pyrochlore phase, as the rather heavy cations are not expected to migrate at the moderate oxidation temperature of 600 °C.

3.3.3. X-ray absorption spectroscopy

Both the 1300 °C and 1400 °C XANES spectra (see Fig. 13) reveal a weakly developed pre-edge around 18005 eV, while the spectrum of the sample treated at 1500 °C indicates a clear pre-edge feature. The pronounced pre-edge feature for the 1500 °C spectrum may be interpreted as a better developed κ-$Ce_2Zr_2O_8$ phase where the Zr atom is coordinated to eight oxide ions which form two sets of distorted tetrahedral with different Zr—O bond lengths. Accordingly, the less pronounced pre-edge feature in the 1300 °C and 1400 °C spectra may be regarded as a less well developed κ-$Ce_2Zr_2O_8$ phase, also in agreement with the results of Rietveld refinement. The peak splitting of the main feature of the 1500 °C spectrum is close to the corresponding spectrum of the cubic ZrO2 [30]. This interpretation of the XANES data suggests that the preparation involving a reductive treatment of the t-$Ce_{0.5}Zr_{0.5}O_2$ phase at 1500 °C to form the pyrochlore represents the optimum conditions for the preparation of the κ-$Ce_2Zr_2O_8$ phase.

The corresponding EXAFS functions are compared with the starting solid solution in Fig. 14a. The curves of samples prepared at 1300–1400 °C are very similar, confirming the resemblance evidenced by the XANES region of the same samples. On the other hand, the curve of the 1500 °C sample shows some differences in particular in the 5–9 Å^{-1} range, which give rise to an increased intensity in the 2–3 Å range of the FT.

The EXAFS functions were fitted in the range 3–16 Å^{-1}, using as starting set of data the results of the Rietveld refinement of the corresponding XRD data (Table 6 and Fig. 14b–d), and taking into account the different phases composition.

According to the previously discussed XRD analysis, in the κ-$Ce_2Zr_2O_8$ phase the local environment around the Zr cations can be interpreted as formed by two sets of distorted tetrahedral configurations. The EXAFS findings confirm that the Zr1 site is more symmetric that the Zr2 one. For the Zr1 coordination shell, two different shells with distorted fourfold coordinations could be detected, presenting each three bonds of similar length and a fourth different one (for detailed model see Table S1). This is in good agreement with corresponding Rietveld refinement in Section 3.3.1. The local environment for the Zr2 is slightly more distorted, with the eight oxygen atoms distributing over 6 different lengths.

With increasing reduction temperature, there is an expansion in the Zr-O distances, as seen also for the pyrochlore case; for example, the Zr$_1$—O distances are spread over the range 1.91–2.31 Å in the
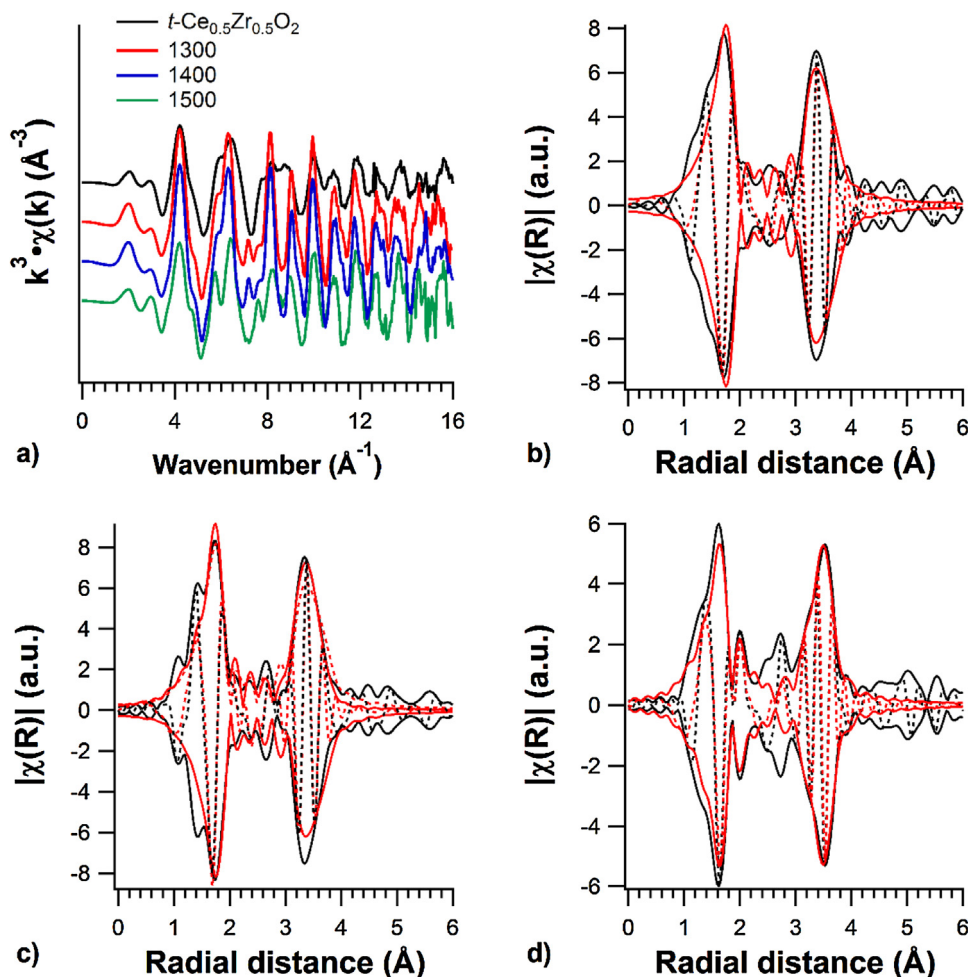
Fig. 14. (a) k^3-weighted EXAFS function and Fourier Transforms with corresponding imaginary parts for κ-$Ce_2Zr_2O_8$ at (b) 1300 °C, (c) 1400 °C and (d) 1500 °C (black: experimental; red: fit; continuous lines: magnitude; dotted lines: imaginary). (For interpretation of the references to colour in this figure legend, the reader is referred to the web version of this article.)

case of the sample reduced at 1300 °C, with the range shifting first to 2.07–2.49 Å (1400 °C) and further to 2.07–2.76 Å (1500 °C). In addition, a further loosely bound oxygen atom can be found in the 1500 °C sample at a distance of about 3.25 Å, which is also present in the refined XRD structure of this sample.

On the contrary, the change in temperature does not induce, in the Zr-cations' second shell, a clear expansion, but rather a rearrangement in the Zr-Zr and Zr-Ce distances, especially around the Zr_2 site. Conversely to the samples reduced at lower temperature, in the 1500 °C sample the Zr cations are on average closer to the scatterer than the Ce ones.

4. Conclusions

In this paper we have prepared the κ-$Ce_2Zr_2O_8$ phase starting from the high temperature reduction of t-$Ce_{0.5}Zr_{0.5}O_2$ solid solution at 1300, 1400, and 1500 °C to form the pyrochlore phase pyr-$Ce_2Zr_2O_7$ followed by mild re-oxidation of the pyrochlore at 600 °C. These three synthesized samples were structurally characterized by XRD, X-ray absorption spectroscopy and Raman spectroscopy. According to XRD, it turns out that temperatures of 1300 °C and maybe even 1400 °C are not sufficient to produce a phase-pure pyrochlore structure pyr-$Ce_2Zr_2O_7$ and κ-$Ce_2Zr_2O_8$ phase. The material obtained by preparation temperatures of 1300 °C is about a 50%:50% mixture of pyrochlore and cubic $Ce_{0.5}Zr_{0.5}O_2$. Reduction at a temperature of 1500 °C is able to form the phase-pure pyrochlore

and κ-$Ce_2Zr_2O_8$ phase. These conclusions are essentially reconciled with XANES and EXAFS analyses and with Raman spectroscopy.

We should note that XRD, XANES/EXAFS and Raman spectroscopy probe different properties of the pyrochlore and the κ-$Ce_2Zr_2O_8$ phase. With XRD we can follow the long-range ordering of the cation sublattice, since the cations are much stronger scatterers than oxygen with respect to X-rays. This fact is also the reason why one can readily detect disorder in the cationic sublattice of the pyrochlore phase pyr-$Ce_2Zr_2O_7$ and the κ-$Ce_2Zr_2O_8$ phase for a preparation temperature of 1300 °C. By contrast, Raman spectroscopy is sensitive towards the ordering of the oxide ion sublattice. From Raman spectroscopy, in particular the broad spectral features, we infer that even for the preparation performed at 1500 °C the anionic sublattice exhibits a high degree of disorder which is removed when mildly re-oxidizing the sample at 600 °C. XANES and EXAFS performed at the Zr K-edge monitors the local oxygen coordination around the Zr cations. Here the pyrochlore phase obtained by treatment at 1400 °C and 1500 °C exhibits a well ordered cubic symmetry with a uniform Zr—O bond length of 2.14 Å which agrees quantitatively with the corresponding value (2.16 Å) obtained by Rietveld refinement obtained from XRD data.

The situation is more complex for the local Zr^{4+} coordination shell of the κ-$Ce_2Zr_2O_8$ phase. Here the Rietveld analyses found two types of ZrO_8 polyhedra which are different in local bond geometry. The Zr(1) coordination shell consists of one undistorted Zr(1)O_4 tetrahedron and one distorted Zr(1)O_4 tetrahedron with three short

Table 6

Fitting of EXAFS data of the κ-$Ce_2Zr_2O_8$ phase prepared at 1300, 1400, and 1500 °C. C.N.: coordination number. Similar bonds are grouped together. Detailed information for each shell, including corresponding Debye-Waller factors, can be found in the supporting information (Table S1).

Sample	Phase	Neighbor	C.N.	Distance (± 0.02) (Å)
1300	κ-$Ce_2Zr_2O_8$ (Zr1)	O1	4	1.91–1.95
	($\Delta E_0 = -7.8 \pm 5.1$)	O2	4	2.17–2.31
		Zr1	3	3.74
		Ce1	6	3.80–3.85
		Zr2	3	3.94
	κ-$Ce_2Zr_2O_8$ (Zr2)	O1	1	1.60
	($\Delta E_0 = -7.8 \pm 5.1$)	O2	3	1.84–2.07
		O3	3	2.31–2.34
		O4	1	2.45
		Ce1/Zr1	1 + 1	3.52–3.54
		Ce2/Zr2	4 + 4	3.64–3.68
		Ce3/Zr3	1 + 1	3.72–3.74
	c-$Ce_{0.5}Zr_{0.5}O_2$	O1	8	2.19
	($\Delta E_0 = 6.0 \pm 1.0$)	Zr1	6	3.91
		Ce1	6	3.91
	t-$Ce_{0.5}Zr_{0.5}O_2$	O1	4	2.11
	($\Delta E_0 = -5.4 \pm 2.7$)	O2	4	2.30
		Ce1/Zr1	6 + 6	3.83
1400	κ-$Ce_2Zr_2O_8$ (Zr1)	O1	4	2.07–2.16
	($\Delta E_0 = 3.6 \pm 1.1$)	O2	4	2.33–2.49
		Zr1	3	3.68
		Ce1	6	3.76–3.79
		Zr2	3	3.83
	κ-$Ce_2Zr_2O_8$ (Zr2)	O1	1	1.70
	($\Delta E_0 = 3.6 \pm 1.1$)	O2	3	1.91–2.14
		O3	3	2.32–2.44
		O4	1	2.50
		Ce1/Zr1	1 + 1	3.56
		Ce2/Zr2	1 + 2	3.65–3.66
		Ce3/Zr3	4 + 2	3.72–3.76
	c-$Ce_{0.5}Zr_{0.5}O_2$	O1	8	2.22
	($\Delta E_0 = 3.1 \pm 1.3$)	Zr1	6	3.86
		Ce1	6	3.75
1500	κ-$Ce_2Zr_2O_8$ (Zr1)	O1	1	2.07
	($\Delta E_0 = -3.3 \pm 1.5$)	O2	6	2.41–2.46
		O3	1	2.76
		Zr1	3	3.60
		Ce1/Zr2	6 + 3	3.81–3.89
	κ-$Ce_2Zr_2O_8$ (Zr2)	O1	1	2.09
	($\Delta E_0 = -3.3 \pm 1.5$)	O2	3	2.17–2.20
		O3	3	2.30–2.32
		O4	1	2.39
		O5	1	3.26
		Zr1	3	3.60–3.68
		Ce1	3	3.77
		Ce2/Zr2	2 + 2	3.80
		Zr3	1	3.85
		Ce3	1	3.91

(2.27 Å) and one long Zr—O bond (2.42 Å). The Zr(2) coordination shell comprises two distorted $Zr(2)O_4$ tetrahedra, exhibiting eight different Zr—O bonds ranging from 1.73 Å to 2.58 Å. These results are consistent with corresponding X-ray absorption experiments. From the Raman data we conclude that the oxide ion sublattice is well ordered.

Preparation at 1500 °C results in the formation of well-defined pyrochlore and κ-$Ce_2Zr_2O_8$ phase. However, due to the high reduction temperature, the average crystallite size is about 80 nm so that the active surface area is below $1\,m^2\,g^{-1}$ which is not acceptable for applications in catalysis. Therefore the active surface area of the κ-$Ce_2Zr_2O_8$ phase prepared at 1500 °C needs to be improved.

Appendix A. Supplementary data

Supplementary data associated with this article can be found, in the online version, at http://dx.doi.org/10.1016/j.apcatb.2016.03.049.

References

[1] A. Trovarelli (Ed.), Catalysis by Ceria and Related Materials, vol. 2, Imperial College Press, London, 2002.

[2] M. Moser, C. Mondelli, T. Schmidt, F. Girgsdies, M.E. Schuster, R. Farra, L. Szentmiklósi, D. Teschner, J. Pérez-Ramírez, Appl. Catal. B 123 (2013) 132–133.

[3] R. Farra, M. Eichelbaum, R. Schlögl, L. Szentmiklósi, T. Schmidt, A.P. Amrute, C. Mondelli, J. Pérez-Ramírez, D. Teschner, J. Catal. 297 (2013) 119–127.

[4] H. Over, R. Schomäcker, ACS Catal. 3 (2013) 1034–1046.

[5] M. Pijolat, M. Prin, M. Soustelle, O. Touret, P. Nortier, J. Chem. Soc. Faraday Trans. 91 (1995) 3941–3948.

[6] J. Kaspar, P. Fornarsiero, M. Graziani, Cat. Today 50 (1999) 285–298.

[7] G. Colon, F. Valdivielso, M. Pijolat, R.T. Baker, J.J. Calvino, S. Bernal, Catal. Today 50 (1999) 271–284.

[8] P. Fornasiero, R. Di Monte, G. Ranga Rao, J. Kaspar, S. Meriani, A. Trovarelli, J. Catal. 151 (1995) 168–177.

[9] R. Di Monti, J. Kaspar, J. Mater. Chem. 15 (2005) 633–648.

[10] A. Trovarelli, Catal. Rev. Sci. 38 (1996) 439–520.

[11] S. Urban, C.H. Kanzler, N. Tarabanko, K. Zalewska-Wierzbicka, R. Ellinghaus, S.F. Rohrlack, L. Chen, P. Klar, B.M. Smarsly, H. Over, Catal. Lett. 143 (2013) 1362–1367.

[12] M. Möller, H. Over, B. Smarsly, N. Tarabanko, S. Urban, Catal. Tod. 253 (2015) 207–218.

[13] S.A. Sadykov, N.N. Sazonova, A.S. Bobin, V.S. Muzykantov, E.L. Gubanova, G.M. Alikina, A.I. Lukashevich, V.A. Rogov, E.N. Ermakova, E.M. Sadovskaya, N.V. Mezentseva, E.G. Zevak, S.A. Veniaminov, M. Muhler, C. Mirodatos, Y. Schuurman, A.C. van Veen, Catal. Today 169 (2011) 125–137.

[14] S. Otsuka-Yao-Matsuo, H. Morikawa, N. Izu, K. Okuda, J. Japan Inst. Met. 12 (1995) 1237–1246.

[15] P. Fornasiero, G. Balducci, R. di Monte, J. Kaspar, V. Sergo, G. Gubiotosa, A. Ferrero, M. Granzinani, J. Catal. 164 (1996) 173–183.

[16] S. Otsuka-Yao-Matsuo, T. Omata, N. Izu, H. Kishimoto, J. Solid State Chem. 138 (1998) 47–54.

[17] H. Kishimoto, T. Omata, S. Otsuka-Yao-Matsuo, K. Ueda, H. Hosono, H. Kawazoe, J. Alloys Comp. 312 (2000) 94–103.

[18] Y. Nagai, T. Yamamoto, T. Tanaka, S. Yoshida, T. Nonaka, T. Okamoto, A. Suda, M. Sugiura, Catal. Today 74 (2002) 225–234.

[19] A. Suda, Y. Ukyo, H. Sobukawa, M. Sugiura, J. Ceram. Soc. Jpn. 110 (2002) 126.

[20] T. Yamamoto, A. Suzuki, Y. Nagai, T. Tanabe, F. Dong, Y. Inada, M. Nomura, M. Tada, Y. Iwasawa, Angew. Chem. Int. Ed. 46 (2007) 9253–9256.

[21] B. de Rivas, R. Lopez-Fonseca, M.A. Gutierrez-Ortiz, J.I. Gutierrez-Ortiz, Catal. Tod. 176 (2011) 470–473.

[22] B. de Rivas, R. Lopez-Fonseca, M.A. Gutierrez-Ortiz, J.I. Gutierrez-Ortiz, Appl. Catal. B: Environ. 101 (2011) 317–325.

[23] J.J. Casey, L. Katz, W.C. Orr, J. Am. Chem. Soc. 77 (1955) 2187–2189.

[24] N.A. Dhas, K.C. Patil, J. Mater. Chem. 3 (1993) 1289–1294.

[25] T. Montini, N. Kickey, P. Fornasiero, M. Granziani, M.A. Banares, M.V. Martinez-Huerta, T. Alessandri, L.E. Depero, Chem. Mater. 17 (2005) 1157–1166.

[26] T. Sasaki, Y. Ukyo, K. Kuroda, S. Arai, S. Muto, H. Saka, J. Ceram. Soc. Jpn. 112 (2004) 440–444.

[27] S. Trasobares, M. Lopez-Haro, M. Kociak, K. March, F. de La Pena, J.A. Perez-Omil, J.J. Calvino, N.R. Lugg, A.J. D'Alfonso, L.J. Allen, Colliex Angew, Chem. Intl. Ed. 50 (2011) 868–872.

[28] M. Lopez-Haro, J.A. Perez-Omil, J.C. Hernandez-Garrido, S. Trasobares, A.B. Hungria, J.M. Cies, P.A. Midgley, P. Bayle-Guillemaud, A. Martinez-Arias, S. Bernal, J.J. Delgado, J.J. Calvino, ChemCatChem 3 (2011) 1015–1027.

[29] T. Alessandri, M.A. Banares, L.E. Depero, M. Ferroni, P. Fornasiero, F.C. Geannari, N. Hickey, M.V. Martinez-Huerta, T. Montini, Top. Catal. 41 (2006) 35–42.

[30] B. Ravel, M. Newville, J. Synchrotron Radiat. 12 (2005) 537–541.

[31] J.C. Hernandez, A.B. Jungria, J.A. Perez-Omil, S. Trasobares, S. Bernal, P.A. Midgley, A. Alavi, J.J. Calvino, J. Phys. Chem. C 111 (2007) 9001–9004.

[32] H.-F. Wang, Y.-L. Guo, G.-Z. Lu, P. Hu, Angew. Chem. Int. Ed. 48 (2009) 8289–8292.

[33] P. Li, I.-W. Chen, J.E. Penner-Hahn, Phys. Rev. B 48 (1993) 10063–10073.

[34] M. Yashima, H. Arashi, M. Kakihana, M. Yoshimura, J. Am. Ceram. Soc. 77 (1994) 1067–1071.

[35] W. Miśta, T. Rayment, J. Hanuza, L. Macalik, Mat. Sci. Pol. 22 (2004) 153–170.

[36] D. Michel, M. Perez y Jorba, R. Collongues, J. Raman Spectrosc. 5 (1976) 163–180.

[37] R.A. McCauley, J. Appl. Phys. 51 (1980) 290–294.

[38] F.W. Poulsen, M. Glerup, P. Holtappels, Solid State Ionics 135 (2000) 595–602.

[39] M. Glerup, O.F. Nielsen, F.W. Poulsen, J. Solid State Chem. 160 (2001) 25–32.

[40] T. Omata, H. Kishimoto, S. Otsuka-Yao-Matsuo, N. Ohtori, N. Umesaki, J. Solid State Chem. 147 (1999) 573–583.

[41] X. Wang, K. Jiang, L. Zhou, J. Nucl. Mater. 458 (2015) 156–161.

[42] T. Masui, Y. Peng, K. Machida, G. Adachi, Chem. Mater. 10 (1998) 4005–4009.

[43] H. Xie, L.L. Wang, D.L. Luo, Y.S. Yang, J. Mater. Sci. 49 (2014) 3314–3321.

[44] D. Errandonea, R.S. Kumar, S.N. Achary, O. Gomis, F.J. Manjon, R. Shukla, A.K. Tyagi, J. Appl. Phys. 111 (2012) 053519.

[45] V.M. Orera, R.I. Merino, F. Peña, SolidState Ionics 72 (1994) 224–231.

[46] J.R. McBride, K.C. Hass, B.D. Poindexter, W.H. Weber, J. Appl. Phys. 76 (1994) 2435–2441.